Large-scale *ab initio* simulations of MAS DNP enhancements using a Monte Carlo optimization strategy

Frédéric A. Perras[a] and Marek Pruski[a,b]*

[a] US DOE, Ames Laboratory, Ames, IA, 50011, USA

[b] Department of Chemistry, Iowa State University, Ames, IA, 50011, USA

*Author to whom correspondence should be addressed: mpruski@iastate.edu

Abstract

Magic-angle-spinning (MAS) dynamic nuclear polarization (DNP) has recently emerged as a powerful technology enabling otherwise unrealistic solid-state NMR experiments. The simulation of DNP processes which might, for example, aid in refining the experimental conditions or the design of better performing polarizing agents, is, however, plagued with significant challenges, often limiting the system size to only 3 spins. Here, we present the first approach to fully *ab initio* large-scale simulations of MAS DNP enhancements. The Landau-Zener equation is used to treat all interactions concerning electron spins, and the low-order correlations in Liouville space (LCL) method is used to accurately treat the spin diffusion, as well as its MAS speed dependence. As the propagator cannot be stored, a Monte Carlo optimization method is used to determine the steady-state enhancement factors. This new software is employed to investigate the MAS speed dependence of the enhancement factors in large spin systems where spin diffusion is of importance, as well as to investigate the impacts of solvent and polarizing agent deuteration on the performance of MAS DNP.

1. Introduction

Owing to recent technological advancements, dynamic nuclear polarization (DNP) has emerged as a superb means of sensitizing NMR spectroscopy, which typically suffers from a low Boltzmann polarization of the nuclei.[1] Simply put, in DNP, unpaired electrons are irradiated near their Larmor frequencies with high-power microwaves in order to transfer their much higher magnetization to the nuclei. This allows for sensitivity enhancements (ε) up to γ_e/γ_n, which corresponds to 658 for ^{1}H. Two major approaches to performing DNP have been developed, magic-angle-spinning (MAS) DNP[1,2,3] and dissolution DNP,[4] which can be used to enhance solid-state and solution-state NMR experiments, respectively.

Generally, the success of a DNP experiment depends on a number of factors, the most important, non-hardware, component being the appropriate deployment of the unpaired electron polarization sources. Numerous procedures for the incorporation of the unpaired electrons into the samples have been proposed, each of which is applicable to a discrete class of materials; for instance, frozen solutions for molecular species and proteins,[5,6] impregnation methods for surfaces,[7,8,9,10] physical incorporation for pharmaceutical formulations[11], and incorporation of metal ion dopants for inorganic materials.[12] These methods all attempt to optimize the contact between the radical polarization source and the target nuclei of interest. Additionally, DNP enhancement factors can be greatly improved by tailoring the quality of the polarizing agent. In MAS DNP, for instance, DNP enhancements have grown by nearly one order of magnitude in recent years by a stepwise optimization of the polarizing agent.[13]

The earliest MAS DNP measurements utilized monoradicals as a polarization source.[14,15] These were then superseded by the invention of biradical polarizing agents, which contain two

tethered radicals whose Larmor frequencies can become separated by the nucleus' Larmor frequency, through MAS, and allow much greater enhancement via an energy conserving three-spin flip transition, referred to as the cross-effect DNP.[16] The biradicals were subsequently improved by shortening the linker connecting the two nitroxide spins,[17] introducing a rigid linker,[18,19] and lastly increasing their molecular weight to lengthen the electron relaxation times.[13,20,21,22,23] A recent *in silico* study of the design of dinitroxide polarization agents has, however, concluded that there is little room remaining for improvement within this family of polarizing agents.[24] Nevertheless, other developments, such as the discovery of the Overhauser effect in insulating solids[25,26,27] and the synthesis of trityl-nitroxide biradicals,[28] promise to greatly improve DNP at ultra-high magnetic fields for which they are already outperforming dinitroxides.[27,28]

A highly efficient *in silico* quantum-mechanical treatment would greatly help in better understanding the mechanisms of MAS DNP and guide further advancements of the technique, but carrying it out over the relevant timescales presents a large computational challenge. This is the case for two reasons. First, one polarizing agent is typically tasked with polarizing thousands of nuclear spins and, since the dimensions of the Hamiltonian scale as 2^N and those of the Liouvillian as 4^N, where N is the number of spins, the problem at hand quickly becomes intractable. As a result of this, all quantum mechanical MAS DNP simulations have, to date, been performed on small spin systems (most consisting only of a single nuclear spin with two electrons).[24,29,30,31,32,33,34] Secondly, DNP is a very slow process, requiring several seconds to reach equilibrium, which nonetheless depends on a series of very rapid (< 1 ns) processes, due to the large sizes of the radical's interactions. The spin dynamics must then be calculated using gargantuan matrices for several seconds in nanosecond increments.

Recently, major strides towards performing large-scale MAS DNP simulations have been put forward by Thurber and Tycko,[35] as well as Mentink-Vigier and co-workers.[36] They discovered that the cross-effect DNP mechanism under MAS conditions operates with a series of three rotation-induced zero crossings termed "rotor events". Microwave rotor events (referred herein as 'MW' events) partially saturate one electron spin when its Larmor frequency equals that of the microwave beam. The D/J events, with D and J denoting electron-electron dipolar and exchange couplings, respectively, occur when the two electrons have equal Larmor frequencies and partially transfer the saturation from one electron to the other. Lastly, cross-effect (CE) events occur when the cross-effect condition is matched and polarization is transferred from the electrons to the nuclei. This discovery led to the realization that the costly spin dynamics of the radicals did not need to be calculated throughout the entirety of the rotor period but that, instead, if their timings were first calculated, the calculation of their spin dynamics could be limited to the time around the rotor event in question. Further simplifications could then be obtained if the population changes occurring during the event were calculated directly using either the Bloch- or Landau-Zener-type equations.[35,36] This formalism then allowed for a dramatic increase in the speed of MAS DNP simulations.

To better represent the experimental situation, Mentink-Vigier and co-workers also explored the possibility of performing MAS DNP simulations on large spin systems, composed of many nuclei and electrons.[36] They applied a phenomenological spin diffusion model to model the interactions between the nuclear spins, while the Bloch/Landau-Zener formalisms were used to calculate the polarization transferred from the electrons to the nearby nuclei. Although very impressive, and a true game changer, this approach to spin diffusion fails to provide a means to explore the many-body spin dynamics involved in DNP since a homogeneous spin diffusion

coefficient is chosen to represent a fundamentally inhomogeneous sample. In order to properly treat the relative rates of spin diffusion between spins with different tensorial orientations and internuclear distances, an *ab initio* quantum mechanical approach is required. This is particularly important in assessing the impact of fast-MAS on the performance of DNP,[37] since the faster spinning would be expected to both reduce the efficiency of DNP as well as slow down the spin diffusion tasked with polarizing the bulk.

To model the spin dynamics involved in DNP to large spin systems, we have decided to apply the restricted state space method of Dumez and coworkers, termed "low-order correlations in Liouville space" (LCL).[38,39,40,41,42,43] Notably, they used LCL to simulate, quantitatively, the spin diffusion in spin systems as large as 144 protons.[38] Similar approaches were also used for the calculation of solution-state NMR data and,[44,45,46,47] more recently, ^{1}H MAS spectra.[48] In this paper, we will describe our implementation of this approach to calculate the DNP enhancements in large spin systems using a Monte Carlo optimization scheme, with our calculations presented alongside the experimental results, for comparison.

It is also important to note that Köckenberger and co-workers have also developed a promising kinetic Monte Carlo approach for the simulation of solid-effect and cross-effect DNP in very large spin systems.[49,50,51] This method has yet to be applied to spinning samples.

2. Theory

In Liouville space, the density matrix (σ) can be expressed as a sum of different basis vectors ($\hat{B}_{\mathrm{r}}$):[40]

$$\sigma(t) = \sum_{\mathrm{r}} b_{\mathrm{r}}(t)\hat{B}_{\mathrm{r}} \,, \qquad (1)$$

where $b_r(t)$ are coefficients and r is simply an index.[52] The basis vectors correspond to products of different single-spin angular momentum operators:

$$\hat{B}_r = 2^{q_r-1}\prod_{i=1}^{N}\hat{I}_{i,r} \tag{2}$$

where q_r is the spin order of the basis vector of index r, which corresponds to the number of spins in the product whose operators do not correspond to identity ($\hat{E}_i$), and $\hat{I}_{i,r}$ is the operator associated with spin i in the product:

$$\hat{I}_{i,r} \in \left\{\hat{E}_i, \hat{I}_{iz}, \frac{\hat{I}_{i+}}{\sqrt{2}}, \frac{\hat{I}_{i-}}{\sqrt{2}}\right\}, \tag{3}$$

Clearly, for the N-spin system the complete basis set then consists of 4^N basis vectors. In Liouville space, however, the size of the basis set can be conveniently reduced by eliminating basis vectors that negligibly affect the calculation. This property of Liouville space calculations has already been used several times for the simulation of DNP processes.[36,49,50,51,53] The first reduction that can be done in order simulate spin diffusion is to keep the basis vectors that have a total coherence order of zero.[40] In other words, the raising and lowering operators in each basis vector need to be balanced ($\hat{I}_{iz}$, $\hat{I}_{iz}\hat{I}_{jz}$, $\hat{I}_{i-}\hat{I}_{j+}$, $\hat{I}_{iz}\hat{I}_{jz}\hat{I}_{kz}$, etc.). The second, primary, assumption used in LCL calculations is that the basis vectors with large q_r can be ignored, which dramatically reduces the size of the Liouvillian. Quantitative agreement between exact and LCL calculations of spin diffusion under MAS conditions can be obtained by considering only basis vectors with a q_r not exceeding 4 or 5.[40,43] It is worth noting that applications of the LCL method have been limited to short spin diffusion timescales and that it is unclear to what extent the higher-order

correlations would impact the results of long spin diffusion simulations. This approximation is also limited to MAS frequencies ranging from 2.5 to 50 kHz.[39,40]

The time dependence of the density matrix can be evaluated using the Liouville-von-Neumann equation:

$$\frac{d\sigma}{dt} = -i\left[\hat{H},\sigma\right] \equiv -i\hat{\hat{L}}\sigma\,, \tag{4}$$

where the commutator between the Hamiltonian and the density matrix is known as the Liouvillian ($\hat{\hat{L}}$). Dumez et al. have conveniently compiled a table listing the different entries of the homonuclear dipolar Liouvillian matrix.[40] Briefly, each basis vector is connected to others having q_r values increased, or decreased, by 1. The size of those non-zero matrix elements is simply equal to the size of the dipolar frequency ($\pm\omega_{D,i,j}$) of the spin pair which gives rise to the transition. In order to calculate $\omega_{D,i,j}$ in a rotating sample it is most convenient to express the dipolar Hamiltonian using spherical tensors, due to their favorable, and well-documented,[54] rotational properties. Within this framework, sequential rotations of the molecular frame can be accomplished by simply multiplying the corresponding irreducible spherical tensor components by Wigner rotation matrices ($D^{l}_{m,m'}$). For the general, powder averaged, MAS case, three sequential rotations need to be performed. We first rotate the crystal frame with respect to the laboratory frame by Euler angles of 0, θ, and φ, (for the powder average), and then rotate individual dipolar vectors by Euler angles of α, β, and γ, to relate them to the crystal frame. Lastly the sample is rotated by Euler angles of $\omega_r t$, $\theta_r = 54.74°$, and 0 to perform magic angle spinning. Within this framework, the $\omega_{D,i,j}$ values can be calculated in straightforward fashion with eq 5.[40]

$$\omega_{\mathrm{D,i,j}}(t) = 2\pi R_{\mathrm{DD}} \sum_{m=-2}^{2} \sum_{m'=-2}^{2} D^2_{0,m}(0,\theta,\phi) D^2_{m,m'}(\alpha,\beta,\gamma) D^2_{m',0}(\omega_{\mathrm{r}} t, \theta_{\mathrm{r}}, 0). \quad (5)$$

In the equation above, R_{DD} is the dipolar coupling constant, defined as

$$R_{\mathrm{DD}} = \left(\frac{\mu_0}{4\pi}\right)\left(\frac{\gamma_{\mathrm{i}}\gamma_{\mathrm{j}}\eta}{2\pi}\right)\left\langle r_{\mathrm{i,j}}^{-3}\right\rangle \quad (6)$$

where γ_i is the gyromagnetic ratio of spin i; and r_{ij} denotes the internuclear distance between spins i and j.

Conventionally, the density matrix is propagated by exponentiating the Liouvillian in order to calculate the propagator ($\hat{\hat{U}}$). The calculation of this exponential is usually the computational bottleneck, as it requires the calculation of time consuming matrix-matrix operations:

$$\sigma(\tau) = \exp\left(-i\tau\hat{\hat{L}}\right)\sigma(0) \equiv \hat{\hat{U}}(0,\tau)\sigma(0). \quad (7)$$

Note that the Liouvillian is time dependent due to the application of magic-angle-spinning; thus, equation 7 needs to be rewritten as follows, if we assume that the Liouvillian is piecewise time-independent:

$$\sigma(\tau) = \hat{T}\prod_{p=0}^{P-1} \exp\left(-i\Delta t \hat{\hat{L}}(t_{\mathrm{p}})\right)\sigma(0), \quad (8)$$

where $\hat{T}$ is the Dyson time-ordering operator and the time from 0 to τ is separated into P time-independent segments. Although the Liouvillian is very sparse and can be stored (in sparse format), the propagator is dense; thus, this approach to propagation cannot be used to treat large

spin systems. Any attempt at calculating the propagator would quickly overrun the memory of the computer. In order to remedy this, Dumez has used the Suzuki-Trotter method to propagate the density matrix, which avoids the storage of the Liouvillian.[39] We have instead made use of the Taylor expansion of the exponential in order to propagate the density matrix using only inexpensive matrix-vector operations without ever calculating the propagator while storing the Liouvillian in sparse format:[44]

$$\exp\left(-i\Delta t\hat{\hat{L}}(t_{\mathrm{p}})\right)\sigma(0)=\sum_{n=0}^{\infty}\frac{(-i\Delta t)^{\mathrm{n}}}{n!}\left(\hat{\hat{L}}(t_{\mathrm{p}})\left(\hat{\hat{L}}(t_{\mathrm{p}})\left(...\left(\hat{\hat{L}}(t_{\mathrm{p}})\sigma(0)\right)\right)\right)\right). \tag{9}$$

Although this approach may seem daunting, MAS forces us to use small time steps; thus, the expansion converges very rapidly such that it only needs to be summed to n=3. Equation 9 then becomes

$$\sigma(t_{\mathrm{p}})=\sigma(0)-i\Delta t\hat{\hat{L}}(t_{\mathrm{p}})\sigma(0)-\frac{\Delta t^{2}}{2}\hat{\hat{L}}(t_{\mathrm{p}})\left(\hat{\hat{L}}(t_{\mathrm{p}})\sigma(0)\right)+\frac{i\Delta t^{3}}{6}\hat{\hat{L}}(t_{\mathrm{p}})\left(\hat{\hat{L}}(t_{\mathrm{p}})\left(\hat{\hat{L}}(t_{\mathrm{p}})\sigma(0)\right)\right). \tag{10}$$

Note that only three matrix-vector operations are needed to propagate the density matrix by Δt. In fact, with this implementation, the computational bottleneck is now the construction of the Liouvillian matrix rather than the calculation of the propagation.

In order to include DNP in the simulation, the product operators for the two electrons involved in the cross-effect need to be added to the basis set. This, however, leads to an increase, by a factor of 16, of the matrix dimensions used for the LCL calculations. Furthermore, due to the large size of the interactions affecting the electrons, which are on the order of hundreds of MHz instead of tens of kHz for the ^{1}H-^{1}H dipolar couplings, much smaller time steps are required in order to accurately reproduce the various rotor events that impact the DNP

efficiency.[33] In total, this approach to simulating DNP in large spin systems would be approximately 6-orders of magnitude more computationally demanding than the already demanding LCL calculations.

We have thus decided to instead combine the LCL method with the Landau-Zener method pioneered for DNP by Thurber and Mentink-Vigier.[35,36] The Landau-Zener formula (LZ) describes the amount of polarization that is transferred between states during a level crossing. These level crossings occur due to the spinning of the rotor, which imparts a time dependence on the EPR frequencies. As mentioned earlier, there are three types of level crossings that are important for cross-effect MAS DNP: (1) D/J events, which exchange populations between electrons due to the dipolar and exchange coupling between them, occur when $\omega_{e,1} - \omega_{e,2} \approx 0$, (2) MW events, which partly saturate an electron when $\omega_e - \omega_{MW} = 0$, and (3) CE events which transfer polarization from the electrons to the nuclei when $\omega_{e,1} - \omega_{e,2} \approx \omega_n$. In multi-spin systems, it is also important to consider a fourth event type, the nuclear-nuclear D/J event which occurs when the hyperfine splittings of two nuclei are equal.[36] This mechanism is responsible for the spin diffusion within the spin diffusion barrier (defined as the volume within a certain distance from the electron spins) as well as between the core nuclei and the bulk nuclei (which are connected among themselves by the homonuclear dipolar coupling Liouvillian). An overview of the model and the interactions connecting the different types of spins is given in Figure 1.

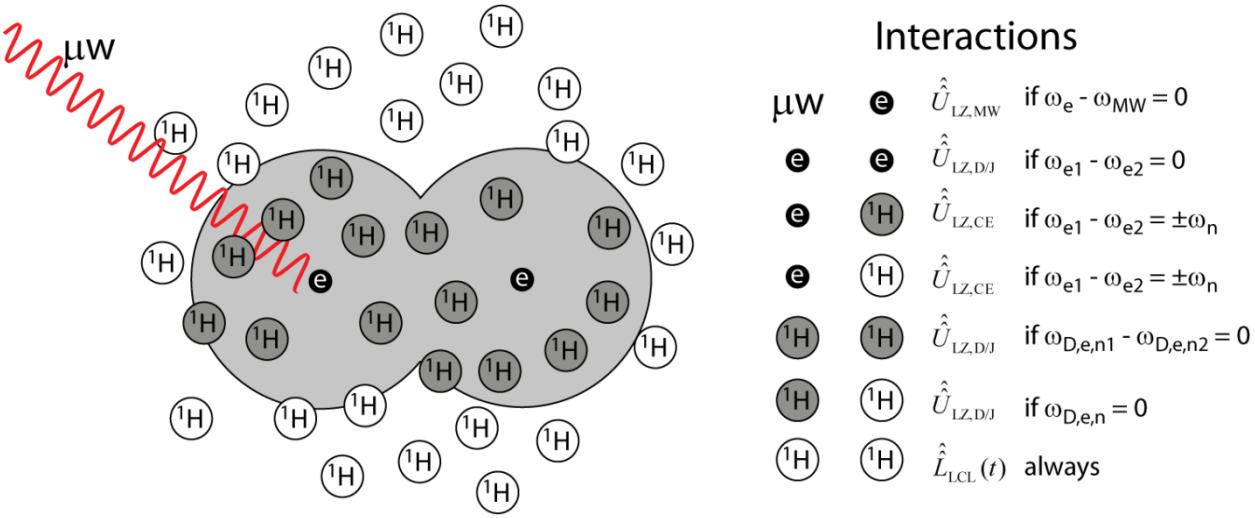

Figure 1. The model used for the calculations consists of two electrons and a bath of different discrete nuclei. The electrons interact with the microwave beam, each other, and all the nuclei using Landau-Zener rotor events. The nuclei are separated into two types, core (grey), and bulk (white) nuclei. The core nuclei are connected to all nuclei by Landau-Zener rotor events, while the bulk nuclei are connected to each other using the LCL formalism.

As shown by Mentink-Vigier,[36] the LZ formulas that operate during the three types of rotor events can be rewritten as propagators in Liouville space such that only the I_z product operators of the two electrons need to be added to the basis set, as well as the identity operator, which is required for the incorporation of relaxation, *vide infra*. A detailed derivation of these propagators is given in the supporting information to reference 36. These are reiterated here in their practical forms used in the simulation code.

The propagator for the D/J events corresponds to the following. Note that the identity operator is given the first index, followed by the two electrons' I_z operators, and finally the LCL basis vectors for the nuclei.

$$\hat{\hat{U}}_{\mathrm{LZ,D/J}}(t_{\mathrm{p}}) = \begin{bmatrix} 1 & 0 & 0 & 0 & \Lambda & 0 \\ 0 & 1-\varepsilon_{\mathrm{D/J}} & \varepsilon_{\mathrm{D/J}} & 0 & \Lambda & 0 \\ 0 & \varepsilon_{\mathrm{D/J}} & 1-\varepsilon_{\mathrm{D/J}} & 0 & \Lambda & 0 \\ 0 & 0 & 0 & 1 & \Lambda & 0 \\ \mathrm{M} & \mathrm{M} & \mathrm{M} & \mathrm{M} & \mathrm{O} & \\ 0 & 0 & 0 & 0 & & 1 \end{bmatrix}, \tag{11}$$

where $\varepsilon_{\mathrm{D/J}}$ is equal to zero when there is no event and:

$$\varepsilon_{\mathrm{D/J}} = 1 - \exp\left(\frac{-\pi\left(\omega_{\mathrm{D,e1,e2}} + 2J_{\mathrm{ex,1,2}}\right)^2}{2\left|\frac{d(\omega_{e,1} - \omega_{e,2})}{dt}\right|} \right), \tag{12}$$

when a D/J event occurs. Note that in the absence of a rotor event, the propagator simply corresponds to the identity matrix and thus, in practice, the propagator can be ignored unless an event takes place. The variable $\omega_{\mathrm{D,e1,e2}}$ corresponds to the dipolar frequency for the coupling between the two electrons, which is calculated using equation 5. J_{ex} corresponds to the isotropic exchange coupling constant between the electrons.

The propagator for the MW events can be written as follows:

$$\hat{\hat{U}}_{\mathrm{LZ,MW}}(t_{\mathrm{p}}) = \begin{bmatrix} 1 & 0 & 0 & 0 & \Lambda & 0 \\ 0 & 1-2\varepsilon_{\mathrm{1,MW}} & 0 & 0 & \Lambda & 0 \\ 0 & 0 & 1-2\varepsilon_{\mathrm{2,MW}} & 0 & \Lambda & 0 \\ 0 & 0 & 0 & 1 & \Lambda & 0 \\ \mathrm{M} & \mathrm{M} & \mathrm{M} & \mathrm{M} & \mathrm{O} & \\ 0 & 0 & 0 & 0 & & 1 \end{bmatrix}, \tag{13}$$

where $\varepsilon_{\mathrm{i,MW}}$ is equal to zero when there is no MW event for electron *i*, and

$$\varepsilon_{\mathrm{i,MW}} = 1 - \exp\left(\frac{-\pi\omega_{\mathrm{1,MW}}^2}{2\left|\frac{d(\omega_{\mathrm{MW}} - \omega_{\mathrm{e,i}})}{dt}\right|} \right), \tag{14}$$

when a MW event occurs, similarly to the *D/J* case. Here, $\omega_{1,\mathrm{MW}}$ corresponds to the microwave power while ω_{MW} is its frequency.

Lastly, the propagator for the cross-effect events is given by:

$$\hat{\hat{U}}_{\mathrm{LZ,CE}}(t_{\mathrm{p}}) = \begin{bmatrix} 1 & 0 & 0 & 0 & \Lambda & 0 & \Lambda & 0 \\ 0 & 3+\varepsilon_{\mathrm{CE}\pm} & 1-\varepsilon_{\mathrm{CE}\pm} & 0 & \Lambda & \pm(1-\varepsilon_{\mathrm{CE}\pm}) & \Lambda & 0 \\ 0 & 1-\varepsilon_{\mathrm{CE}\pm} & 3+\varepsilon_{\mathrm{CE}\pm} & 0 & \Lambda & \mu(1-\varepsilon_{\mathrm{CE}\pm}) & \Lambda & 0 \\ 0 & 0 & 0 & 1 & \Lambda & 0 & \Lambda & 0 \\ \mathrm{M} & \mathrm{M} & \mathrm{M} & \mathrm{M} & \mathrm{O} & \Lambda & \Lambda & 0 \\ 0 & \pm(1-\varepsilon_{\mathrm{CE}\pm}) & \mu(1-\varepsilon_{\mathrm{CE}\pm}) & 0 & \mathrm{M} & 3+\varepsilon_{\mathrm{CE}\pm} & \Lambda & 0 \\ \mathrm{M} & \mathrm{M} & \mathrm{M} & \mathrm{M} & \mathrm{M} & \mathrm{M} & \mathrm{O} & 0 \\ 0 & 0 & 0 & 0 & 0 & 0 & 0 & 1 \end{bmatrix}, \tag{15}$$

where CE+ refers to the cross-effect events of the type $\omega_{1,\mathrm{e}}$- $\omega_{2,\mathrm{e}} = \omega_{\mathrm{n}}$ and CE- refers to cross-effect events of the type $\omega_{1,\mathrm{e}}$- $\omega_{2,\mathrm{e}} = -\omega_{\mathrm{n}}$. Note that the CE rotor events, for a given electron pair, occur simultaneously for all nuclei of a given isotope, and thus the corresponding matrix-vector operation needs to be repeated for each nucleus:

$$\sigma(t_{\mathrm{p}}) = \prod_{i=0}^{N-1}\left(\hat{\hat{U}}_{\mathrm{LZ,CE,i}}\right)\sigma(0) \tag{16}$$

The use of this first-order Suzuki-Trotter approximation is justified given that CE events transfer only very minute quantities of electron polarization. In equation 15, $\varepsilon_{\mathrm{CE}\pm}$ is given by

$$\varepsilon_{\mathrm{CE}\pm} = 2\exp\left(\frac{-\pi\left|h_{\mathrm{x}}^{\mathrm{CE}}\right|^2 \omega_{\mathrm{D,e1,e2}}}{2\omega_{\mathrm{n}}\left|\frac{d\left(\omega_{\mathrm{e,1}} - \omega_{\mathrm{e,2}}\ \mathrm{m}\omega_{\mathrm{n}}\right)}{dt}\right|}\right) - 1, \tag{17}$$

where the $h_{\mathrm{x}}^{\mathrm{CE}}$ term is given by:

$$h_{\mathrm{x}}^{\mathrm{CE}} = \sqrt{A_{zx}^2 + A_{zy}^2}\,\omega_{\mathrm{D,e1,e2}} / \omega_{\mathrm{n}}\,. \tag{18}$$

with $\sqrt{A_{zx}^2 + A_{zy}^2}$ being the pseudo-secular term of the hyperfine coupling Hamiltonian to the first electron. For simplicity in implementation, this term is calculated as:

$$\sqrt{A_{\mathrm{zx}}^2 + A_{\mathrm{zy}}^2} = \frac{3}{2} A_{\mathrm{zz}} \cos\vartheta \sqrt{\left(\cos^2\vartheta - 1\right)}, \tag{19}$$

where A_{zz} is the hyperfine coupling constant, calculated using equation 6, and

$$\cos\vartheta = \sqrt{\frac{2\sum_{m=-2}^{2}\sum_{m'=-2}^{2} D_{0,m}^2(0,\theta,\phi) D_{m,m'}^2(\alpha,\beta,\gamma) D_{m',0}^2(\omega_{\mathrm{r}}t,\theta_{\mathrm{r}},0) + 1}{3}}\,. \tag{20}$$

A derivation of equations 19-20 is given in the supporting information. The last important piece that is needed in order to calculate the DNP enhancement is relaxation. This can be done by simply including a phenomenological relaxation superoperator ($\hat{\hat{R}}_{1,2}$), which has the general form:

$$\exp(\Delta t\hat{\hat{R}}_{1,2}) = \begin{bmatrix} 1 & 0 & \mathrm{L} \\ b_{\mathrm{r,eq}}\left(1 - e^{\sum_n -\Delta t/T_{\mathrm{n}}}\right) & e^{\sum_n -\Delta t/T_{\mathrm{n}}} & \mathrm{L} \\ \mathrm{L} & \mathrm{L} & \mathrm{O} \end{bmatrix}. \tag{21}$$

In equation 21, $b_{r,eq}$ is the equilibrium value of a given basis vector. It is simply set to 658 for the two electrons' I_z basis vectors, 1 for the nuclei's I_z basis vectors and 0 for all the others. T_n corresponds to the relaxation time of a given product operator, which is equal to T_1 for each spin with an I_z propagator and T_2 for the raising and lowering operators. Note that the basis vectors with high q_r, which are ignored in LCL calculations, in fact relax much faster,[55] which further supports the validity of the LCL approximation.[56]

At each time step the density matrix is calculated using

$$\sigma(t_p) = \exp(\Delta t \hat{\hat{R}}_{1,2}) \hat{\hat{U}}_{LZ,CE} \hat{\hat{U}}_{LZ,MW} \hat{\hat{U}}_{LZ,D/J} \hat{\hat{U}}_{LCL} \sigma(0), \quad (22)$$

which is calculated as follows to minimize the memory requirements and completely avoid all matrix-matrix operations:

$$\sigma(t_p) = \exp(\Delta t \hat{\hat{R}}_{1,2}) \hat{U}_{LZ,CE} \hat{U}_{LZ,MW} \hat{U}_{LZ,D/J} \left(\sigma(0) - i\Delta t \hat{L}(t_p)\sigma(0) - \frac{\Delta t^2}{2} \hat{L}(t_p)\left(\hat{L}(t_p)\sigma(0) \right) + \frac{i\Delta t^3}{6} \hat{L}(t_p)\left(\hat{L}(t_p)\left(\hat{L}(t_p)\sigma(0) \right) \right) \right). \quad (23)$$

Conventionally in DNP-MAS simulations,[32] the propagator for a rotor period is stored as

$$\hat{\hat{U}}_{rotor} = \prod_{t=0}^{t_r} \exp(\Delta t \hat{\hat{R}}_{1,2}) \hat{\hat{U}}_{LZ,CE}(t_r) \hat{\hat{U}}_{LZ,MW}(t_r) \hat{\hat{U}}_{LZ,D/J}(t_r) \hat{\hat{U}}_{LCL}(t_r), \quad (24)$$

which can then be reused to rapidly calculate the polarizations at any rotor period, or calculate the pseudo-steady-state[42] polarizations:

$$\sigma(\infty) = \left(\hat{\hat{U}}_{rotor} \right)^{\infty} \sigma(0). \quad (25)$$

Unfortunately, this cannot be done in the large-scale case since a propagator of these matrix dimensions cannot be stored, or even calculated. It would seem that equation 23 would

need to be repeated to infinity in order to calculate DNP enhancements using this approach. In order to circumvent this, we have chosen to use an optimization strategy to quickly converge on the pseudo-steady-state populations. We opted to use a Monte Carlo-type optimization algorithm for this purpose (see Figure 2).

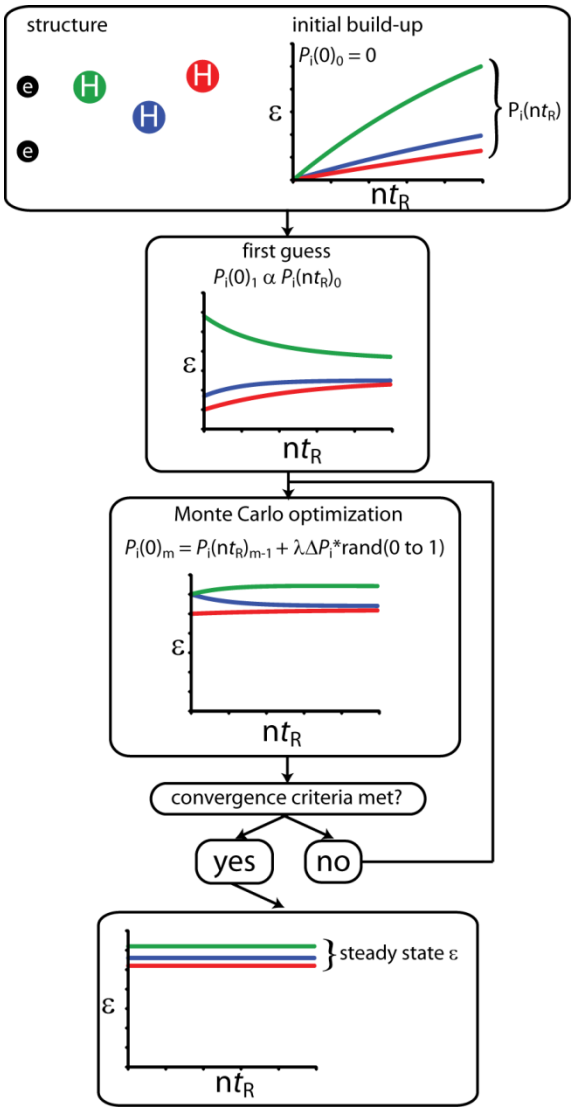

Figure 2. Flowchart depicting the Monte Carlo optimization scheme used to determine the steady-state DNP enhancement factors. First, the nuclear polarizations are set to zero and the density matrix is propagated over a short period of time to determine the initial build-up rates. The nuclear polarizations are then reset to new values that are proportional to those build-up rates and the density matrix is propagated once again. A random step of the nuclear

polarizations is then taken, according to equation 27, and the density matrix is propagated once more. This last process is repeated until the nuclear polarizations have converged.

Briefly, an initial guess of the steady-state polarizations is taken. The nature of this guess is relatively inconsequential, given that there are no local minima, and will only impact the speed of the convergence. For simplicity we have set our initial polarizations proportionally to their initial DNP build-up rates, such that they are also in the expected range of enhancements (calculated using equation 23 with the initial polarizations set to zero). The density matrix is then propagated, using equation 23, over a fixed number of rotor periods in order to assess the direction of change (ΔP) (increase vs. decrease) in polarization,

$$\mathbf{\Delta P} = \begin{bmatrix} \pm 1 & \pm 1 & \text{L} & \pm 1 \end{bmatrix}. \tag{26}$$

Typically a single rotor period was sufficient to determine $\mathbf{\Delta P}$, however, the use of a greater number of rotor periods can be beneficial if the spin diffusion is slow. The size of the polarization gradient is not taken into consideration since the DNP and spin diffusion processes have very different time scales which can lead to considerable convergence problems when using alternative algorithms that make explicit use of gradients.

A random step in polarization is then taken in this direction to generate new polarizations, and the density matrix is propagated once more:

$$\mathbf{P}(0)_m = \mathbf{P}(nt_R)_{m-1} + \lambda \mathbf{\Delta P} \begin{bmatrix} rand(0\ to\ 1) \\ rand(0\ to\ 1) \\ \text{M} \\ rand(0\ to\ 1) \end{bmatrix}. \tag{27}$$

This is repeated until the polarizations of all nuclei have converged to within a certain criterion. In general, we obtained stable convergence by setting the maximum step size (λ) to 30-15 and then decreasing it to 2-0.5 enhancement units as the optimization proceeds. An average over the last 5 time steps is then taken. When this average converges to ±0.5 enhancement units over multiple cycles, the optimization ends. Note that this approach converges much faster than typical Monte Carlo methods since the direction in which to take the random step is always known. We found that, for most of the models studied here, between 20 and 100 optimization steps were required to converge the DNP enhancements with the larger models taking proportionally longer to converge, with the proportionality factor being roughly equal to N. Since the LCL method scales as N^4, this method roughly scales as N^5, with N being the number of bulk ^{1}H spins in the system. The largest model considered here (btbk-d0 with 33 additional bulk protons, *vide infra*) required 251 optimization steps to converge, and took 5 days of computation time of a 4-core i5-4590 processor. Improvements in the optimization algorithm are certain to greatly impact the speed at which these calculations are performed, as well as the size of the systems that can be investigated.

Powder averaging was implemented using both spherical and REPULSION grids.[57,58] REPULSION was found to converge significantly faster, requiring only 66 α, β pairs and 2 γ angles in order to converge. To reduce the number of independent variables, the optimization routine was performed on the powder-averaged polarizations of each spin, as opposed to those of the individual isochromats. Both approaches would yield the same powder-averaged steady-state. This theory was implemented into parallelized C code that uses the GNU Scientific Library (GSL) for the sparse matrix storage and manipulation. Most calculations were performed on a

desktop PC with a 4-core, 2.30 GHz, AMD Phenom X4 processor while the larger calculations were performed on 12-core, 2.00 GHz, Intel Xeon E5-2620 processors.

3. Results and Discussion

3.1 Spinning speed dependence

It is generally understood that only the few nuclei in the immediate vicinity of the electron spins are efficiently polarized by DNP and that it is the spin diffusion that carries this hyperpolarization to the remainder of the bulk nuclei.[36,59] One of the major advantages of the software described here is its ability to properly treat the effects of MAS on spin diffusion. This, in turn, should offer greater insights than the previously used 3-spin models into the MAS speed dependence of the DNP enhancement, a topic that has been very heavily studied. In the following sections, we will calculate the enhancements using several spin models and investigate the effects associated with deuteration of the solvent and the polarizing agent.

3.1.1 Spin diffusion

The role of spin diffusion is particularly important when microcrystalline or amorphous bulk solids are studied, as the radicals are unable to penetrate the sample and directly polarize the nuclei in its core.[60,61] Since there is an obvious interest in applying DNP to the studies of glasses, semiconductor nanoparticles,[62] narrow-pore materials (such as metal-organic frameworks, MOFs),[63,64,65,66,67] pharmaceuticals,[11,68,69,70] biological materials,[71,72,73] and other non-penetrable solids,[60] which often have very long relaxation times that allow for the storage of hyperpolarization,[74] it is important to address the impact that fast-MAS will have on this field.

As such, we have measured the DNP experimental enhancement factors ($\varepsilon_{expt.}$), as a function of the MAS frequency (ν_R), for both a 16 mM TEKPol[13] solution of 1,1,2,2-tetrachloroethane (TCE), where a homogeneous radical distribution is expected, as well as a sample of sucrose impregnated with a 16 mM TEKPol solution in deuterated TCE, using a Bruker 1.3-mm fast-MAS DNP probe. The enhancement factors were measured at $15 \leq \nu_R \leq 40$ kHz (15 kHz being the slowest stable spinning frequency of this probe) and are plotted in Figure 3.

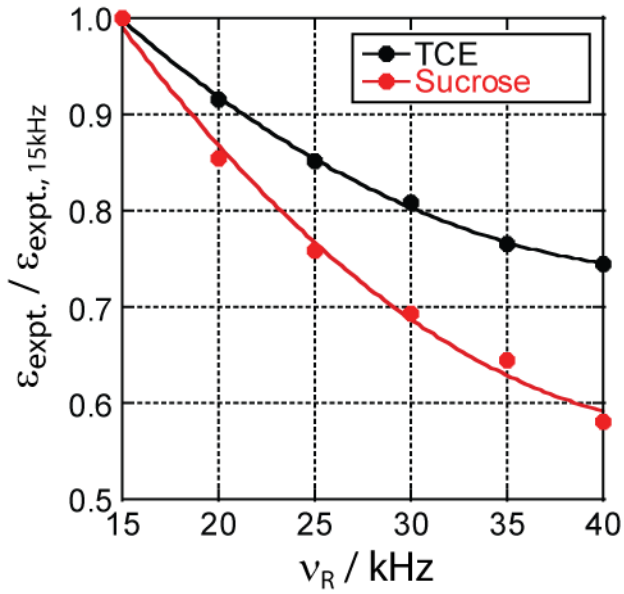

Figure 3. The relative enhancement factors of a TCE solution of TEKPol and a microcrystalline sucrose sample impregnated with a solution of TEKPol in deuterated TCE. Due to the longer distance required for the spin diffusion in the sucrose sample, the enhancement factors drop more quickly.

As expected, the enhancement factors for both samples decrease as a function of ν_R but the drop is much steeper for sucrose. This is the case since spin polarization must diffuse much further in a microcrystalline solid. The penetration depth of the hyperpolarization is generally controlled by the spin diffusion rate and the T_1 relaxation time of the ^{1}H nuclei in the sample,[60,61,75] which is very long for sucrose (~700 s). In spite of the very long relaxation time,

the spin diffusion rate is significantly decreased at 40 kHz which harms the enhancement factors for this microcrystalline solid. This will of course be an important factor to consider in the future, since the application of fast MAS to microcrystalline solids is very desirable as it would lead to an increase in spectral resolution and the opportunity to implement ^{1}H-detected heteronuclear correlation schemes.

We have sought to explore this *in silico* and see whether our software would be able to reproduce these experimental results and lend further theoretical insights into the transfer of polarization to the bulk. For this purpose, we adopted as a model a linear chain[32,76] of 11 nuclear spins. This model is well-suited to study the polarization of nuclei since the single path for polarization transfer both simplifies the analysis and also slows down the spin diffusion, making it easier to distinguish changes in polarization. Note that the slowed spin diffusion in this model may be in part caused by its high symmetry, a known shortcoming of the LCL method.[42] However, in the spin system considered here this symmetry is broken by the introduction of the electron spins.

The two electrons were separated by 10.5 Å and the first ^{1}H spin was located 2.5 Å from one of the electrons (similar to the nearest hydrogen atom in TEMPO). The remaining 10 ^{1}H spins were separated by 2 Å steps. A relatively short T_1 relaxation time of 1 s was given to all the ^{1}H nuclei to accentuate the effects. Both electrons had identical g-tensor principal components of g_{xx} = 2.00194, g_{yy} = 2.00614, and g_{zz} = 2.00988,[33] with the tensors oriented with Euler angles of $\alpha = \beta = \gamma = 90°$, J_{ex} = 25 MHz, and T_{1e} values of 300 μs, in agreement with a dinitroxide.[24] The microwave beam had a frequency of 263.45 MHz, which is optimal for a ^{1}H Larmor frequency of 400 MHz, and a power of 850 kHz. In all cases the rotor period was separated into 200 discrete time-independent increments for the calculation.

Calculations were performed with and without a spin diffusion barrier in order to assess its impact on the enhancements, as well as its dependence on the spinning frequency, including the hypothesis that the spin diffusion barrier dissipates under MAS.[32,36] The results of these simulations are depicted in Figure 4. As can be seen, in the absence of a spin diffusion barrier, where all nuclei are treated using LCL, the calculated enhancement factors ($\varepsilon_{calc.}$) are seen to gradually decrease as the distance from the electron is increased. As expected, the decline of $\varepsilon_{calc.}$ is more acute at higher ν_R values. When the spin diffusion barrier was properly included, however, we saw a much steeper drop in polarization from the first spin due to the slowed spin diffusion within the barrier, a clear indication that the spin diffusion barrier is indeed operative under MAS. In this case, the $\varepsilon_{calc.}$ values increased at higher ν_R rates, since the nuclear *D/J* rotor events became more frequent. The polarizations of the bulk nuclei, however, dropped as a function of ν_R. The initial increase in porosity of the barrier as the spinning frequency is increased may lead to a shift of the optimal ν_R to a higher value than would be predicted using a 3-spin model.

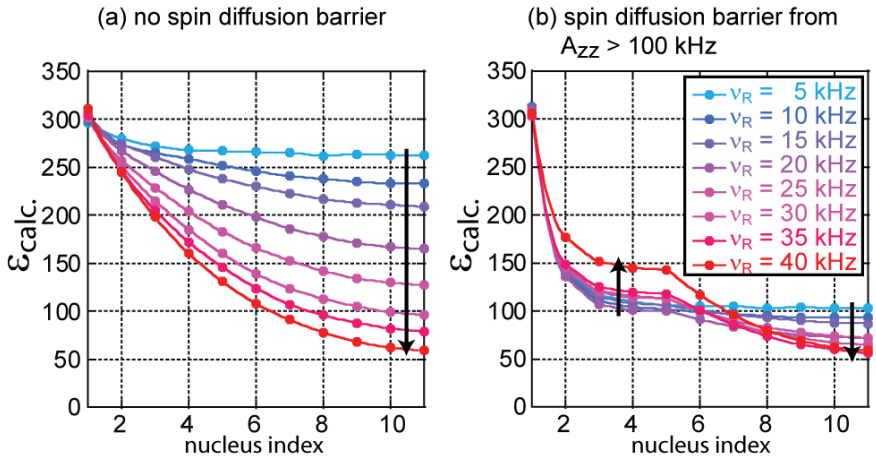

Figure 4. The calculated enhancement factors for a linear 11-spin model as a function of the spinning frequency (5 kHz ≤ ν_R ≤ 40 kHz, see legend in (b) for color assignments), calculated

without the spin diffusion barrier (a) and with one set to $A_{zz} > 100$ kHz (b) in agreement with ref 77.

The results from the calculations depicted in Figure 4b also offer an important prediction regarding the optimal sample formulations for fast-MAS DNP. Given that the enhancement of the nearby nuclei increases while that of the distant spins progressively decreases with ν_R, it follows that in fast-MAS regime there is an even greater need of concentrating the observed nuclei near the polarization source. To verify this experimentally, we have measured the DNP enhancement of TCE impregnated into MCM-41 as a function of ν_R, analogously to the measurements in Figure 3. We tested two concentrations: 16 mM and 32 mM, the first having previously been determined as optimal for this material at MAS rates typically used with 3.2-mm rotors (~10 kHz).[78,79] For the lower concentration of TEKPol, the enhancement factor dropped by 36 %, from 45 to 29, as ν_R was increased from 15 to 35 kHz; however, the resistance to faster spinning almost doubled at 32 mM, as the enhancement factor only dropped by 19%, from 75 to 61. These experimental measurements therefore support the predictions made by our simulations that a higher radical concentration should be used when performing DNP under fast-MAS. In fact, when adjusted for differences in signal quenching and relaxation times, the sensitivity is 78% higher when a radical concentration of 32 mM is used rather than 16 mM for this sample at 35 kHz MAS.

3.1.2 Partial deuteration of the solvent

Recently, there has been interest in the suppression of the solvent resonances in order to obtain cleaner 1D and 2D NMR spectra using DNP. Various approaches have made use of dipolar recoupling,[80] differences in relaxation properties,[81] and even completely removing the solvent.[82,83] A particularly attractive option, due to its generality, is to simply use partially or

fully deuterated solvents, an approach that has long been used in solution-state NMR.[84] However, the spin density decreases as the sample is deuterated, which inevitably leads to a decrease in the spin diffusion rate. This fact is likely to detrimentally affect the applicability of this approach to solvent suppression under fast-MAS conditions. To investigate experimentally whether this is indeed the case, we measured the $\varepsilon_{expt.}$ values as a function of ν_R for three 16 mM solutions of the TEKPol biradical[13] in fully protonated and partially deuterated (50 and 90%) TCE. The results (Figure 5) show that the enhancements dropped far more steeply in the deuterated samples, likely due to the slower spin diffusion. The use of a deuterated solvent when performing DNP under fast MAS may therefore lead to a costly decrease in sensitivity, particularly when also considering the losses due to the lower sample quantity present in rotors with smaller diameter.[85]

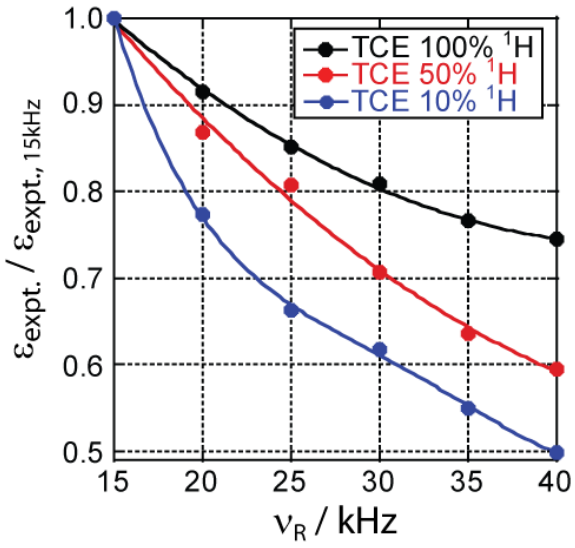

Figure 5. The relative DNP enhancement factors for three TEKPol/TCE solutions with solvent protonation levels of 100 (black), 50 (red), and 10% (blue) are plotted as a function of the spinning frequency.

In order to investigate this *in silico*, we adopted a model consisting of a biradical molecule and a cluster of 25 ^{1}H spins extending away from one of the biradical molecule's

electron spins. Solvent deuteration was mimicked by simply increasing the relative distances between all the nuclei, and thus enlarging the spatial size of the cluster, while keeping the nearest ^{1}H's position constant, at 2.5 Å from the radical. This approach eliminates most variables, such that all changes in enhancement factors can be associated to the change in ^{1}H density itself. Note that the choice of the nearest distance to the radical likely has a very large impact on the results. The coordinates used in the base model are given in Table S1 and the explicit models from the simulations are shown in Figures S1-S5 in the supporting information.

In agreement with the previous work,[60] the T_1 relaxation times of all nuclei were set in accordance to their proximity to the radicals following an r^{-6} dependence:

$$\frac{1}{T_1} = \frac{1}{T_{1,\text{bulk}}} + \sum_{\text{electrons}} \frac{1\text{Å}^6}{T_{1,1\text{Å}} r^6}, \tag{28}$$

where $T_{1,\text{bulk}}$ was set to 20 s and $T_{1,1\text{Å}}$ was set to 1 ms. Note that $T_{1,1\text{Å}}$ corresponds to the T_1 relaxation time of a ^{1}H spin located 1 Å away from the electron. The parameters of the electron spins were kept unchanged from those in section 3.1.1. Note that, for a 16 mM biradical concentration, each biradical molecule is responsible for polarizing an ellipsoid with a volume of approximately 100 nm^3; thus, all spins situated further than 26 Å from the electrons were removed from the simulation model. This helped to limit the number of bulk ^{1}H spins in the model.

In the case of the model having a ^{1}H density of 100% TCE, spin diffusion was sufficiently fast to equilibrate most of the polarization of the bulk spins. As the spinning speed was increased, however, the spin diffusion barrier became more permeable (see also Figure 4b) and the enhancement factors of the bulk spins increased. A larger model is likely needed to

reproduce the experimental result from Figure 5. Note that in all cases the enhancement of the spins near the radical increased with ν_R (not shown) due to the increased permeability of the spin diffusion barrier. For this reason, in Figure 6 we plotted the average $\varepsilon_{calc.}$ values for the more distant spins (distance greater than 15 Å from a radical), as these are expected to better represent the bulk spins that are observed experimentally. These spins can be seen in the models shown in Figures S1-S5 in the supporting information.

For the sample having an 80% ^{1}H density, spin diffusion within the bulk slowed down while the spin diffusion from the core again sped up as ν_R was increased. As a result, the $\varepsilon_{calc.}$ values for the distant ^{1}H spins were largely ν_R-independent. Interestingly, these values show a maximum at ν_R = 30 kHz, where the polarization lost from the slower spin diffusion within the bulk was balanced by the more permeable spin diffusion barrier.

In the case of the samples with ^{1}H concentrations of 60 and 40%, spin diffusion was much slower than spin-lattice relaxation, and 35-50% drops in the average enhancement factors of the distant protons were calculated for increases of ν_R from 5 to 40 kHz, in agreement with the experimental results.

Lastly, in the sample with the lowest ^{1}H concentration (20%), the spin diffusion was effectively quenched and the $\varepsilon_{calc.}$ values were largely ν_R-independent, showing only slight drops due to the lessened efficiency of the cross-effect mechanism at higher MAS frequencies. This clearly confirms that a threshold level ^{1}H density is required in order to mediate the spin diffusion. Importantly, this also demonstrates that in the case of heteronuclei, which possess far weaker homonuclear dipolar couplings than ^{1}H, spin diffusion is not expected to be an important

variable in DNP, with direct DNP transfers dominating the polarization transfers. Note that this may not be the case if the T_1 relaxation times are very long.

It is important to note that although the data presented in Figure 6 show the enhancement factors decreasing with lower ^{1}H density, in larger spin systems the size of the ^{1}H bath will also become an important variable, effectively diluting the hyperpolarization among all spins.[24] Consequently, in spite of the reduced spin diffusion, higher enhancement factors are often observed when a partially deuterated sample is used.[84,86,87,88]

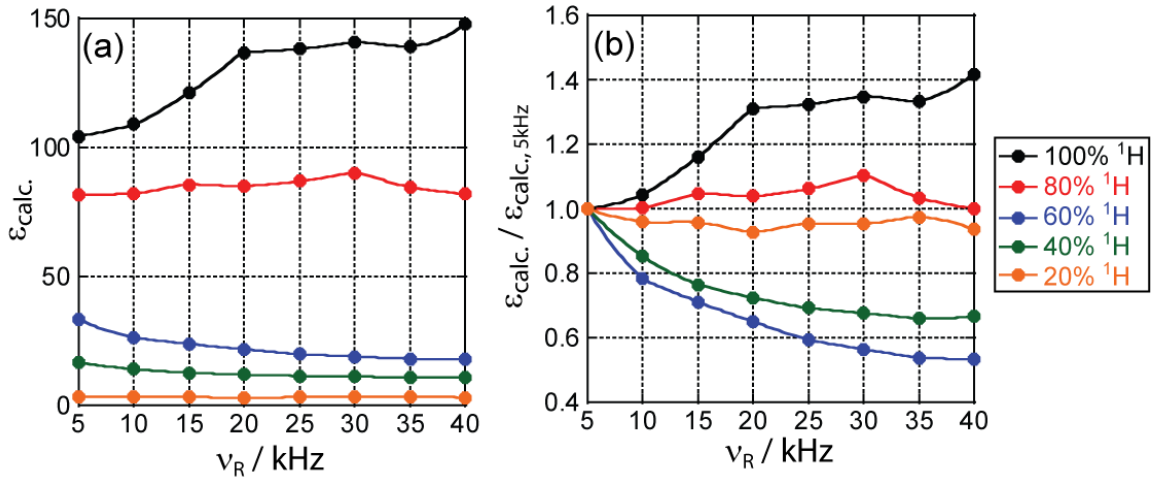

Figure 6. (a) Plot of the average calculated enhancement factors for the distant ^{1}H spins in a cluster containing 25 ^{1}H spins with a density comparable to TCE and the nearest ^{1}H spin situated at 2.5 Å from the radical. These same enhancement factors are plotted in (b) while normalized to the enhancement factor calculated for 5 kHz MAS.

3.2 Biradical Deuteration

Recently, we,[89] as well as others,[22,90] have shown that the performance of a biradical polarizing agent could be improved by deuteration. Two hypotheses were proposed to explain this phenomenon. First, deuteration was seen to lead to an increase in the electron's spin-lattice relaxation time, T_{1e}, which is expected to increase the saturation factor and in turn the enhancement factors. It was also hypothesized that deuteration could improve the performance

by removing the rapidly relaxing core ^{1}H spins that can act as a polarization sink. These possibilities have also been brought forth by many other researchers.[13,77,91,92]

Our new software now allows us to finally investigate these mechanistic questions and determine the reason for the higher DNP performance of deuterated biradical polarizing agents. We first investigated the DNP enhancements corresponding to a btbk molecule[18] in a vacuum, the molecular structure for which is depicted in Figure 7a. The previously derived molecular crystal structure[93] was used, the T_{1e} relaxation times were set to those measured experimentally,[89] and the T_{1n} relaxation times were set according to equation 28. The exchange interaction was set to 0 MHz and ν_R was fixed at 10 kHz. Calculations were performed for the three partially-protonated btbk variants we synthesized (see Figure 7a), denoted as btbk-d0 (corresponding to natural abundance of ^{1}H), btbk-d8 (20% deuterated) and btbk-d32 (80% deuterated). The results of these calculations are tabulated in Table S2 and are compared in Figure 7bi to the enhancement factors measured experimentally in our earlier study.[89]

Interestingly, the calculated results failed to reproduce the experimental finding that increases in partial deuteration lead to an increase in enhancement factors. In fact, the opposite correlation was observed (Figure 7bi). One potential explanation for this result is that the slower relaxing spins of the linker were removed in the case of btbk-d8 (see Figure 7a), which shortened the overall time available for polarization transfer, while all nearby ^{1}H spins were removed in btbk-d32, and we had to then rely on longer-range direct DNP. It would then appear that both nearby ^{1}H spins, and distant, slowly-relaxing, ^{1}H spins are needed for a good DNP performance. An additional, worrisome, conclusion of this result is that small models, such as the popular 3-spin (2 electrons and 1 proton) model, can in fact produce incorrect results and fail to reproduce experimental trends. Clearly, larger-scale DNP simulations, using methods such as the one

described here or previously-proposed quantum-classical models,[36] need to be performed in order to reliably design radical polarizing agents *in silico*.

We then decided to employ a larger model consisting of the biradical molecule and a cluster of 33 ^{1}H spins situated near one of the electrons (see Figure 8). In order to reduce the computational demand, only half of the ^{1}H spins from the symmetric btbk molecule were considered for these simulations. The coordinates of the nuclear and electron spins considered for these calculations are listed in Table S2, along with the $\varepsilon_{calc.}$ values in each of the models. Again, the enhancement factors of the biradical's protons did not correlate to the experimental values ones (see Figure 7bii). Most importantly, however, the factors calculated for the bulk spins did indeed follow the experimental trends. This, again, demonstrates the need to use large models to reproduce experimental results.

In order to gain additional insights into the origins of the improvement in enhancement we performed a calculation in which the btbk-d0 molecule was given the T_{1e} value of btbk-d40. This modification led to an increase in $\varepsilon_{calc.}$ from 152 to 200 (see Table 1), but this enhancement was still lower than that obtained using btbk-d40 (211). This then suggests that the increase in T_{1e} contributes the most to the improvements in DNP performance but that losses in polarization to the rapidly-relaxing ^{1}H spins of the biradical molecule also contribute to the changes in DNP performance, adding validity to the 'polarization sink' hypothesis. Note that our calculated enhancement factors still, however, overestimate the experimental ones. This could be caused by the still too-small model, or a potentially inappropriate ^{1}H distribution. One interesting avenue for improving the quantitative aspect of the simulations would be to combine this method with molecular dynamics to obtain more accurate atomic coordinates.

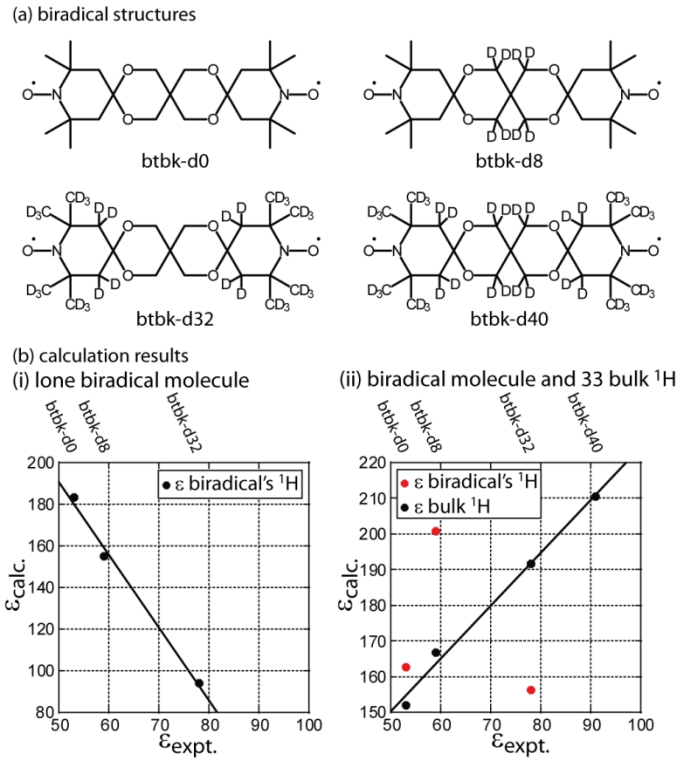

Figure 7. (a) Structures of the four partially-deuterated btbk variants studied.[89] (b) Calculated DNP enhancement factors are plotted as a function of the experimental enhancement factors reported in reference 89 for the 4 partially deuterated btbk variants. In (i), the results for a lone btbk molecule in a vacuum are shown while in (ii), 33 bulk protons were added to the model. In (ii), the red circles correspond to the enhancement factors of the btbk molecule's ^{1}H spins while the black circles correspond to the enhancement factors of the bulk.

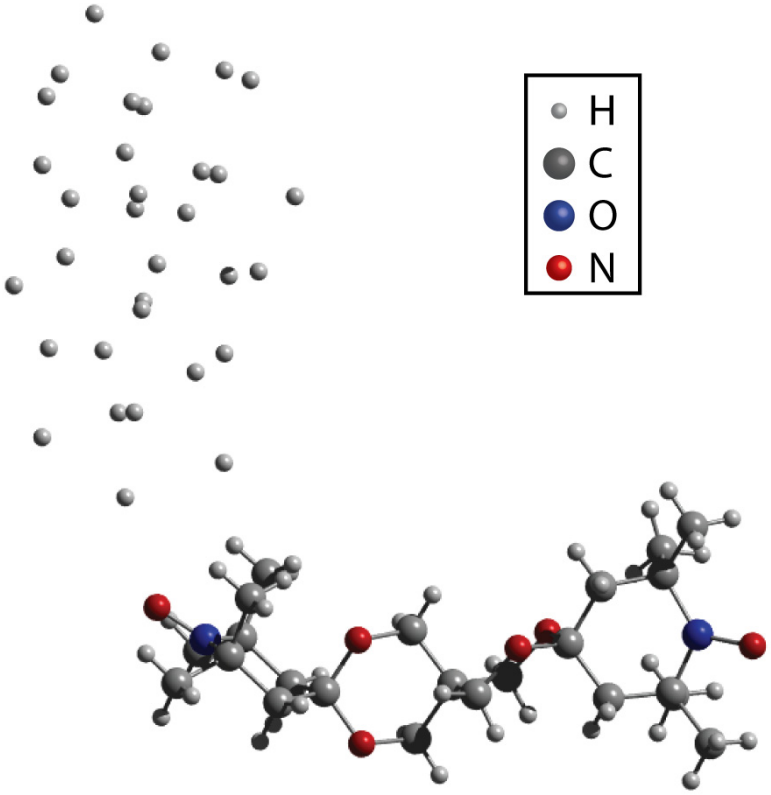

Figure 8. Structural model used to simulate DNP performance in btbk/TCE solutions. ^{1}H spins from the molecule were selectively removed to simulate deuteration according to the text and Table S2.

Table 1. Calculated average DNP enhancement factors for the bulk and biradical ^{1}H spins

structure	T_{1e} / μs[a]	$\varepsilon_{calc.}$(biradical)	$\varepsilon_{calc.}$(bulk)
btbk-d0	35	183	
btbk-d8	62	155	
btbk-d32	87	94	
btbk-d0 with bulk	35	163	152
btbk-d8 with bulk	62	201	167
btbk-d32 with bulk	87	156	192
btbk-d40 with bulk	121		211
btbk-d0 with bulk	121	207	200

[a]The T_{1e} values correspond to the experimentally-determined ones from ref. 89.

4. Conclusions

We have presented a theoretical model that merges the Landau-Zener approach to MAS DNP simulations with the LCL MAS spin diffusion method in order to accurately calculate DNP enhancement factors in large spin systems. Unlike previous phenomenological models, this theory is purely *ab initio* and allows for the influences of the MAS spinning frequency on the spin diffusion rates and DNP processes to be assessed. Contrary to previous theoretical studies of DNP, the build-up of polarization is not calculated and no propagators associated with rotor cycles are stored. This was necessary given the size of the matrices involved in these quantum mechanical spin dynamics simulations. Instead, a Monte Carlo-type optimization was used in order to determine the steady-state polarizations of all the nuclei.

Simulations performed as a function of the MAS frequency in linear chains of ^{1}H spins unequivocally showed that faster MAS frequencies are detrimental to DNP in microcrystalline samples. This finding was corroborated by experiment. Furthermore, the simulations also showed that the spin diffusion barrier still has a large influence on the DNP enhancements under MAS conditions with the spin diffusion from the core accelerating as a function of MAS frequency while the spin diffusion outside the spin diffusion barrier slows down.

Simulations and experiments were also performed in order to investigate the influence of solvent deuteration on the DNP enhancement factors of the nuclei. As expected, more heavily deuterated solutions led to greater losses in polarization under fast MAS. At the highest deuteration levels, spin diffusion was effectively quenched and the nuclei needed to rely solely on direct DNP. This is thus expected to be important for heteronuclei, as they possess far weaker homonuclear dipolar coupling constants.

Lastly, large-scale simulations using this software were able to reproduce the experimental trends observed when the polarizing agent btbk is deuterated. Importantly, simulations consisting of only the polarizing agent in a vacuum failed to reproduce the experimental trends, thus highlighting that larger, more physically reasonable, structural models than have been used to date are needed in order to reproduce experiment. It is expected that improvements in theoretical models, optimization schemes, and implementation, beyond that presented here, will soon enable the *ab initio* simulation of MAS DNP in spin systems consisting of hundreds of nuclei.

5. Experimental

All MAS DNP measurements were performed using a Bruker AVANCE III 400 spectrometer equipped with a 263.7 GHz gyrotron and a 1.3-mm LTMAS probe. The samples were packed into 1.3-mm o.d. zirconia rotors, capped with Vespel caps, pre-spun at room temperature and then finally spun at a temperature of c.a. 110 K for the DNP measurements. ^{1}H Bloch decay experiments were used to measure the enhancement factors using an excitation pulse lasting 2.5 μs. The relaxation delay was set to 1.3 times the DNP build-up time (the average DNP build-up time was used for sucrose, for which a biexponential build-up was observed) and a total of 8-64 scans were accumulated with the microwaves turned on and off. The reported enhancement factors correspond to the intensity ratios of those two experiments.

Acknowledgements

We would like to thank Dr. Jean-Nicolas Dumez, Dr. Takeshi Kobayashi, and Prof. Aaron J. Rossini for many useful discussions. This research was supported by the U.S. Department of Energy (DOE), Office of Science, Basic Energy Sciences, Materials Science and

Engineering Division. The Ames Laboratory is operated for the DOE by Iowa State University under Contract No. DE-AC02-07CH11358. F.P. thanks NSERC (Natural Sciences and Engineering Research Council of Canada) and the Government of Canada for a Banting Postdoctoral Fellowship.

References

1. L. R. Becerra, G. J. Gerfen, R. J. Temkin, D. J. Singel, and R. G. Griffin, Phys. Rev. Lett. **71**, 3561 (1993).
2. T. Maly, G. T. Debelouchina, V. S. Bajaj, K.-N. Hu, C.-G. Joo, M. L. Mak-Jurkauskas, J. R. Sirigiri, P. C. A. van der Wel, J. Herzfeld, R. J. Temkin, and R. G. Griffin, J. Chem. Phys. **128**, 052211 (2008).
3. M. Rosay, L. Tometich, S. Pawsey, R. Bader, R. Schauwecker, M. Blank, P. M. Borchard, S. R. Cauffman, K. L. Felch, R. T. Weber, R. J. Temkin, R. G. Griffin, and W. E. Maas, Phys. Chem. Chem. Phys. **12** 5850 (2010).
4. J. H. Ardenkjaer-Larsen, B. Fridlund, A. Gram, G. Hansson, L. Hansson, M. H. Lerche, R. Servin, M. Thaning, and K. Goldman, Proc. Natl. Acad. Sci. USA **100**, 10158 (2003).
5. M. Rosay, J. C. Lansing, K. C. Haddad, W. W. Bachovchin, J. Herzfeld, R. J. Temkin, and R. G. Griffin, J. Am. Chem. Soc. **125**, 13626 (2003).
6. A. B. Barnes, B. Corzilius, M. L. Mak-Jurkauskas, L. B. Andreas, V. S. Bajaj, Y. Matsuki, M. L. Belenky, J. Lugtenburg, J. R. Sirigiri, R. J. Temkin, J. Herzfeld, and R. G. Griffin, Phys. Chem. Chem. Phys. **12**, 5861 (2010).
7. A. Lesage, M. Lelli, D. Gajan, M. A. Caporini, V. Vitzthum, P. Miéville, J. Alauzun, A. Roussey, C. Thieuleux, A. Mehdi, G. Bodenhausen, C. Copéret, and L. Emsley, J. Am. Chem. Soc. **132**, 15459 (2010).

8. A. J. Rossini, A. Zagdoun, M. Lelli, A. Lesage, C. Copéret, and L. Emsley, Acc. Chem. Res. **46**, 1942 (2013).

9. T. Kobayashi, F. A. Perras, I. I. Slowing, A. D. Sadow, and M. Pruski, ACS Catal. **5**, 7055 (2015).

10. C. Copéret, W.-C. Liao, C. P. Gordon, and T.-C. Ong, J. Am. Chem. Soc. **139**, 10588 (2017).

11. Q. Z. Ni, F. Yang, T. V. Can, I. V. Sergeyev, S. M. D'Addio, S. K. Jawla, Y. Li, M. P. Lipert, W. Xu, R. T. Williamson, A. Leone, R. G. Griffin, and Y. Su, J. Phys. Chem. B **121**, 8132 (2017).

12. T. Chakrabarty, N. Goldin, A. Feintuch, L. Houben, M. Leskes, ChemPhysChem, in press (2018).

13. A. Zagdoun, G. Casano, O. Ouari, M. Schwarzwälder, A. J. Rossini, F. Aussenac, M. Yulikov, G. Jeschke, C. Copéret, A. Lesage, P. Tordo, and L. Emsley, J. Am. Chem. Soc. **135**, 12790 (2013).

14. G. J. Gerfen, L. R. Becerra, D. A. Hall, R. G. Griffin, R. J. Temkin, and D. J. Singel, J. Chem. Phys. **102**, 9494 (1995).

15. M. Rosay, V. Weis, K. E. Kreischer, R. J. Temkin, and R. G. Griffin, J. Am. Chem. Soc. **124**, 3214 (2002).

16. K.-N. Hu, H.-h. Yu, T. M. Swager, and R. G. Griffin, J. Am. Chem. Soc. **126**, 10844 (2004).

17. C. Song, K.-N. Hu, C.-G. Joo, T. M. Swager, and R. G. Griffin, J. Am. Chem. Soc. **128**, 11385 (2006).

18. Y. Matsuki, T. Maly, O. Ouari, H. Karoui, F. Le Moigne, E. Rizzato, S. Lyubenova, J. Herzfeld, T. Prisner, P. Tordo, and R. G. Griffin, Angew. Chem. Int. Ed. **48**, 4996 (2009).

19. M. K. Kiesewetter, B. Corzilius, A. A. Smith, R. G. Griffin, and T. M. Swager, J. Am. Chem. Soc. **134**, 4537 (2012).

20. A. Zagdoun, G. Casano, O. Ouari, G. Lapadula, A. J. Rossini, M. Lelli, M. Baffert, D. Gajan, L. Veyre, W. E. Maas, M. Rosay, R. T. Weber, C. Thieuleux, C. Coperet, A. Lesage, P. Tordo, and L. Emsley, J. Am. Chem. Soc. **134**, 2284 (2012).

21. C. Sauvée, M. Rosay, G. Casano, F. Aussenac, R. T. Weber, O. Ouari, and P. Tordo, Angew. Chem. Int. Ed. **125**, 11058 (2013).

22. D. J. Kubicki, G. Casano, M. Schwarzwälder, S. Abel, C. Sauvée, K. Ganesan, M. Yulikov, A. J. Rossini, G. Jeschke, C. Copéret, A. Lesage, P. Tordo, O. Ouari, and L. Emsley, Chem. Sci. **7**, 550 (2016).

23. C. Sauvée, G. Casano, S. Abel, A. Rockenbauer, D. Akhmetzyanov, H. Karoui, D. Siri, F. Aussenac, W. Maas, R. T. Weber, T. Prisner, M. Rosay, P. Tordo, and O. Ouari, Chem. Eur. J. **22**, 5598 (2016).

24. F. A. Perras, A. D. Sadow, and M. Pruski, ChemPhysChem, **18**, 2279 (2017).

25. T. V. Can, M. A. Caporini, F. Mentink-Vigier, B. Corzilius, J. J. Walish, M. Rosay, W. E. Maas, M. Baldus, S. Vega, T. M. Swager, and R. G. Griffin, J. Chem. Phys. **141**, 064202 (2014).

26. M. Lelli, S. R. Chauhari, D. Gajan, G. Casano, A. J. Rossini, O. Ouari, P. Tordo, A. Lesage, and L. Emsley, J. Am. Chem. Soc. **137**, 14558 (2015).

27. S. R. Chaudhari, D. Wisser, A. C. Pinon, P. Berruyer, D. Gajan, P. Tordo, O. Ouari, C. Reiter, F. Engelke, C. Copéret, M. Lelli, A. Lesage, and L. Emsley, J. Am. Chem. Soc. **139**, 10609 (2017).

28. G. Mathies, M. A. Caporini, V. K. Michaelis, Y. Liu, K.-N. Hu, D. Mance, J. L. Zweier, M. Rosay, M. Baldus, and R. G. Griffin, Angew. Chem. Int. Ed. **54**, 11770 (2015).

29. K. R. Thurber and R. Tycko, J. Chem. Phys. **137**, 084508 (2012).

30. F. Mentink-Vigier, Ü. Akbey, Y. Hovav, S. Vega, and H. Oschkinat, J. Magn. Reson **224**, 13 (2012).

31. F. Mentink-Vigier, S. Paul, D. Lee, A. Feintuch, S. Hediger, S. Vega, and G. de Paëpe, Phys. Chem. Chem. Phys. **17**, 21824 (2015).

32. F. Mentink-Vigier, Ü. Akbey, H. Oschkinat, S. Vega, and A. Feintuch, J. Magn. Reson. **258**, 102 (2015).

33. D. Mance, P. Gast, M. Huber, M. Baldus, and K. L. Ivanov, J. Chem. Phys. **142**, 234201 (2015).

34. P. Gast, D. Mance, E. Zurlo, K. L. Ivanov, M. Baldus, and M. Huber, Phys. Chem. Chem. Phys. **19**, 3777 (2017).

35. K. R. Thurber and R. Tycko, J. Chem. Phys. **140**, 184201 (2014).

36. F. Mentink-Vigier, S. Vega, and G. De Paëpe, Phys. Chem. Chem. Phys. **19**, 3506 (2017).

37. S. R. Chaudhari, P. Berruyer, D. Gajan, C. Reiter, F. Engelke, D. L. Silverio, C. Copéret, M. Lelli, A. Lesage, and L. Emsley, Phys. Chem. Chem. Phys. **18**, 10616 (2016).

38. M. C. Butler, J.-N. Dumez, and L. Emsley, Chem. Phys. Lett. **477**, 377 (2009).

39. J.-N. Dumez, M. C. Butler, E. Salager, B. Elena-Herrmann, and L. Emsley, Phys. Chem. Chem. Phys. **12**, 9172 (2010).

40. J.-N. Dumez, M. C. Butler, and L. Emsley, J. Chem. Phys. **133**, 224501 (2010).

41. J.-N. Dumez, M. E. Halse, M. C. Butler, and L. Emsley, Phys. Chem. Chem. Phys. **14**, 86 (2012).

42. M. E. Halse, J.-N. Dumez, and L. Emsley, J. Chem. Phys. **136**, 224511 (2012).

43. M. E. Halse, A. Zagdoun, J.-N. Dumez, and L. Emsley, J. Magn. Reson. **254**, 48 (2015).

44 I. Kuprov, N. Wagner-Rundell, P. J. Hore, J. Magn. Reson. **189**, 241 (2007).

45 I. Kuprov, J. Magn. Reson. **195**, 45 (2008).

46. H. J. Hogben, M. Krzystyniak, G. T. P. Charnock, P. J. Hore, and I. Kuprov, J. Magn. Reson. **208**, 179 (2011).

47. L. J. Edwards, D. V. Savostyanov, Z. T. Welderufael, D. Lee, I. Kuprov, J. Magn. Reson. **243**, 107 (2014).

48. U. Sternberg, R. Witter, I. Kuprov, J. M. Lamley, A. Oss, J. R. Lewandowski, A. Samoson, J. Magn. Reson. **291**, 32 (2018).

49. A. Karabanov, D. Wiśniewski, I. Lesanovsky, and W. Köckenberger, Phys. Rev. Lett. **115**, 020404 (2015).

50. D. Wiśniewski, A. Karabanov, I. Lesanovsky, and W. Köckenberger, J. Magn. Reson. **264**, 30 (2016).

51. A. Karabanov, D. Wiśniewski, F. Raimondi, I. Lesanovsky, and W. Köckenberger, Phys. Rev. A **97**, 031404 (2018).

52. The index, *r*, is calculated using a similar method as that used by Halse (see reference 42) by grouping particular product operators according to their type (number of raising, lowering, and z operators) and cycling over the operators of that group. These indices are calculated once and then stored for rapid access.

53. A. Karabanov, A. van der Drift, L. J. Edwards, I. Kuprov, and W. Köckenberger, Phys. Chem. Chem. Phys. **14**, 2658 (2012).

54. L. J. Mueller, Concepts Magn. Reson. A **38**, 221 (2011).

55. T. Karlsson, A. Brinkmann, P. J. E. Verdegem, J. Lugtenburg, and M. H. Levitt, Solid State Nucl. Magn. Reson. **14**, 43 (1999).

56. A. Karabanov, I. Kuprov, G. T. P. Charnock, A. van der Drift, L. J. Edwards, W. Köckenberger, J. Chem. Phys. **135**, 084106 (2011).

57. M. Bak and N. C. Nielsen, J. Magn. Reson. **125**, 132 (1997).

58. M. Edén, Concepts Magn. Reson. A **18**, 24 (2003).

59. K.-N. Hu, G. T. Debelouchina, A. A. Smith, and R. G. Griffin, J. Chem. Phys. **134**, 125105 (2011).

60. A. J. Rossini, A. Zagdoun, F. Hegner, M. Schwarzwälder, D. Gajan, C. Copéret, A. Lesage, and L. Emsley, J. Am. Chem. Soc. **134**, 16899 (2012).

61. A. C. Pinon, J. Schlagnitweit, P. Berruyer, A. J. Rossini, M. Lelli, E. Socie, M. Tang, T. Pham, A. Lesage, S. Schantz, and L. Emsley, J. Phys. Chem. C **121**, 15993 (2017).

62. L. Piveteau, T.-C. Ong, A. J. Rossini, L. Emsley, C. Copéret, and M. V. Kovalenko, J. Am. Chem. Soc. **137**, 13964 (2015).

63. A. J. Rossini, A. Zagdoun, M. lelli, J. Canivet, S. Aguado, O. Ouari, P. Tordo, M. Rosay, W. E. Maas, C. Copéret, D. Farrusseng, L. Emsley, and A. Lesage, Angew. Chem. Int. Ed. **51**, 123 (2012).

64. F. Pourpoint, A. S. L. Thankamony, C. Volkringer, T. Loiseau, J. Trébosc, F. Aussenac, D. Carnevale, G. Bodenhausen, H. Vézin, O. Lafon, and J.-P. Amoureux, Chem. Commun. **50**, 933 (2014).

65. Z. Guo, T. Kobayashi, L.-L. Wang, T. W. Goh, C. Xiao, M. A. Caporini, M. Rosay, D. D. Johnson, M. Pruski, and W. Huang, Chem. Eur. J. **20**, 16308 (2014).

66. T. K. Todorova, X. Rozanska, C. Gervais, A. Legrand, L. N. Ho, P. Berruyer, A. Lesage, L. Emsley, D. Farrusseng, J. Canivet, and C. Mellot-Draznieks, Chem. Eur. J. **22**, 16531 (2016).

67. T. Kobayashi, F. A. Perras, T. W. Goh, T. L. Metz, W. Huang, and M. Pruski, J. Phys. Chem. Lett. **7**, 2322 (2016).

68. A. J. Rossini, C. M. Widdifield, A. Zagdoun, M. Lelli, M. Schwarzwälder, C. Copéret, A. Lesage, and L. Emsley, J. Am. Chem. Soc. **136**, 2324 (2014).

69. J. Voger-Gravel, A. Schantz, A. C. Pinon, A. J. Rossini, S. Schantz, L. Emsley, J. Phys. Chem. B **122**, 2073 (2018).

70. L. Zhao, M. P. Hanrahan, P. Chakravarty, A. G. DiPasquale, L. E. Sirois, K. Nagapudi, J. W. Lubach, and A. J. Rossini, Cryst. Growth Des. **18**, 2588 (2018).

71. P. C. A. avn der Wel, K.-N. Hu, J. Lewandowski, R. G. Griffin, J. Am. Chem. Soc. **128**, 10840 (2006).

72. C. Leroy, F. Aussenac, L. Bonhomme-Coury, A. Osaka, S. Hayakawa, F. Babonneau, C. Coelho-Diogo, C. Bonhomme, Anal. Chem. **89**, 10201 (2017).

73. F. A. Perras, H. Luo, X. Zhang, N. S. Mosier, M. Pruski, and M. M. Abu-Omar, J. Phys. Chem. A **212**, 623 (2017).

74. X. Ji, A. Bornet, B. Vuichoud, J. Milani, D. Gajan, A. J. Rossini, L. Emsley, G. Bodenhausen, and S. Jannin, Nature Commun. **8**, 13975 (2017).

75. O. Lafon, A. S. L. Thankamony, T. Kobayashi, D. Carnevale, V. Vitzthum, I. I. Slowing, K. Kandel, H. Vezin, J.-P. Amoureux, G. Bodenhausen, and M. Pruski, J. Phys. Chem. C **117**, 1375 (2013).

76. Y. Hovav, A. Feintuch, and S. Vega, J. Chem. Phys. **134**, 074509 (2011).

77. C. Ramanathan, Appl. Magn. Reson. **34**, 409 (2008).

78. A. J. Rossini, A. Zagdoun, M. Lelli, D. Gajan, F. Rascón, M. Rosay, W. E. Maas, C. Copéret, A. Lesage, L. Emsley, Chem. Sci. **3**, 108 (2012).

79. F. A. Perras, L.-L. Wang, J. S. Manzano, U. Chaudhary, N. N. Opembe, D. D. Johnson, I. I. Slowing, M. Pruski, Curr. Opin. Colloid Interface Sci. **33**, 9 (2018).

80. D. Lee, S. R. Chaudhari, and G. De Paëpe, J. Magn. Reson. **278**, 60 (2017).

81. J. R. Yarava, S. R. Chaudhari, A. J. Rossini, A. Lesage, and L. Emsley, J. Magn. Reson. **277**, 149 (2017).

82. H. Takahashi, D. Lee, L. Dubois, M. Bardet, S. Hediger, and G. De Paëpe, Angew. Chem. Int. Ed. **51**, 11766 (2012).

83. H. Takahashi, S. Hediger, and G. De Paëpe, *Chem. Commun.* **49**, 9479 (2013).

84. T. Kobayashi, F. A. Perras, U. Chaudhary, I. I. Slowing, W. Huang, A. D. Sadow, and M. Pruski, Solid State Nucl. Magn. Reson. **87**, 38 (2017).

85. Y. Nishiyama, Solid State Nucl. Magn. Reson. **78**, 24 (2016).

86. K.-N. Hu, V. S. Bajaj, M. Rosay, and R. G. Griffin, J. Chem. Phys. **126**, 044512 (2007).

87. Ü. Akbey, W. T. Franks, A. Linden, S. Lange, R. G. Griffin, B.-J. van Rossum, and H. Oschkinat, Angew. Chem. Int. Ed. **49**, 7803 (2010).

88. A. Zagdoun, A. J. Rossini, M. P. Conley, W. R. Grüning, M. Schwarzwälder, M. Lelli, W. T. Franks, H. Oschkinat, C. Copéret, L. Emsley, and A. Lesage, Angew. Chem. Int. Ed. **52**, 1222 (2013).

89. F. A. Perras, R. R. Reinig, I. I. Slowing, A. D. Sadow, and M. Pruski, Phys. Chem. Chem. Phys. **18**, 65 (2016).

90. M.-A. Geiger, M. Orwick-Rydmark, K. Märker, W. T. Franks, D. Akhmetzyanov, D. Stöppler, M. Zinke, E. Specker, M. Nazaré, A. Diehl, B.-J. van Rossum, F. Aussenac, T. Prisner, Ü. Akbey, H. Oschkinat, Phys. Chem. Chem. Phys. **18**, 30696 (2016).

91. A. A. Smith, B. Corzilius, A. B. Barnes, T. Maly, and R. G. Griffin, J. Chem. Phys. **136**, 015101 (2012).

92. B. Corzilius, A. A. Smith, and R. G. Griffin, J. Chem. Phys. **137**, 054201 (2012).

93. D. Bardelang, M. Giorgi, V. Hornebecq, A. Stepanov, M. Hardy, E. Rizzato, V. Monnier, M. B. Zaman, G. Chan, K. Udachin, G. Enright, P. Tordo, and O. Ouari, Cryst. Growth Des. **14**, 467 (2014).